Available online at www.sciencedirect.com

ScienceDirect

IFAC PapersOnline CONFERENCE PAPER ARCHIVE

IFAC PapersOnLine 55-20 (2022) 241–246

Parameter Uncertainty Analysis in Precise Pointing Control of Flexible Spacecraft ⋆

János Bezsilla *,** **Béla Takarics** * **Bálint Vanek** * **Jian Guo** **

* *Systems and Control Laboratory, ELKH Institute for Computer Science and Control, Budapest, Hungary*

** *Faculty of Aerospace Engineering, Delft University of Technology, Delft, The Netherlands*

Abstract: This article focuses on the validation of a classical PID controller scheme for flexible spacecraft with regards to the effect of parameter uncertainty on system stability and pointing precision. A high-fidelity simulation environment with external disturbances was built in Simulink using a control-oriented model of an Earth-observing satellite with a flexible appendage and on-board microvibration sources in orbit around the planet. Then, a PID control loop was designed with sensor dynamics, time delay behaviour, and a smooth trajectory generator. After declaring the natural frequencies, damping ratio, and rotation angle of the appendage, as well as the propellant tank mass to be uncertain, two worst-case scenarios were identified. Comparing the response of worst-case systems with nominal settings, only a minor drop has been found in the phase margins, with little to no difference in the pointing errors (smaller than ±2 arcsec for both roll and pitch).

Keywords: flexible spacecraft, nonlinear dynamics, attitude tracking, precise pointing control, PID control, parameter uncertainty

1. INTRODUCTION

Nowadays, there are many ongoing and proposed missions involving spacecraft where extremely accurate pointing is required, either for cosmic vision or Earth observation purposes. These applications usually require rigid vehicles, otherwise a number of disturbing effects would severely impact image quality and line-of-sight stability, such as flexible appendages and internal microvibration sources.

Flexible appendages tend to be prevalent in complex missions, as payload mass restrictions can often only be met with low stiffness structures. Their vibration characteristics are imprecisely known because the gravity environment on Earth does not allow for rigorous testing. This uncertainty of frequency and damping of the flexible modes and potential coupling between axes leads to major challenges in attitude determination and control system (ADCS) design (Gasbarri et al. (2012)). Additionally, manufacturing imperfections in reaction wheels generate residual harmonic microvibrations which can be amplified on interaction with the structure of the spacecraft, leading to failure (Preda et al. (2018)).

In scientific literature of the past decades, one can find a vast number of solutions to these dynamical challenges. Notable examples are the sliding mode controller in Xiao et al. (2011) and the estimator-based method in Xiao et al. (2016), but there are also robust approaches such as Preda et al. (2018) that deal with pointing performance. However, there have been few publications featuring nonlinear models or uncertainty, and just a handful on the verification and validation of these systems, the most impactful ones being Wang et al. (2010) and Gasbarri et al. (2012).

The presented work aims to tackle the control problem of stabilizing the flexible system, while also fulfilling stringent pointing precision requirements and validating the control algorithm for parameter uncertainty. This is achieved by building a simulation environment where the modeled spacecraft is subject to external and internal disturbances. The main contribution of this paper is combining controller validation with a nonlinear test environment that is higher fidelity than most current approaches. The developed simulation environment can be used as a solid basis for achieving more complex goals in the future, such as advanced control design or conducting Monte Carlo campaigns.

This paper is structured as follows: Section 2 presents details on the control-oriented system model as well as the nonlinear equations of motion. Section 3 introduces the proposed control design together with sensor models, and a quaternion-based method for smooth and precise trajectory generation. Based on this design, Section 4 deals with the implications of parameter uncertainty in a exhaustive search of value ranges for four variables. Conclusions are stated in Section 5 at the end of the paper.

⋆ This work was supported in part by the FLiPASED Project, which has received funding from the Horizon 2020 Research and Innovation Programme of the European Union under Grant 815058, and in part by the Ministry of Innovation and Technology NRDI Office within the framework of the Autonomous Systems National Laboratory Program. Supported by the ÚNKP-21-5 New National Excellence Program of the Ministry for Innovation and Technology from the source of the National Research, Development and Innovation Fund. This paper was supported by the János Bolyai Research Scholarship of the Hungarian Academy of Sciences.

10.1016/j.ifacol.2022.09.102

2. MODELLING OF THE NONLINEAR SYSTEM

To describe and analyze the dynamics of the nonlinear system, we built a control-oriented mathematical model in Simulink. Throughout the paper, Sentinel-2B, a European Earth observation satellite is used as a reference spacecraft for both orbit modeling and system characteristics. This features a rotating solar panel, a variable-mass propellant tank, and a spacecraft bus with similar size and mass, presented for the nominal case in table 1.

Table 1. Reference spacecraft parameters

Part	Size (m)	Mass (kg)	Center of mass (m)
Bus	$[3.4; 1.8; 2.35]$	975	$[0; 0; 0]$
Panel	$[0.01; 3.1; 2.3]$	40	$[0; -2.45; 0]$
Tank	$[0.5; 0.5; 0.5]$	125	$[-1.4; 0; 0]$
Sum	-	1140	$[-0.1535; -0.0860; 0]$

Ahead of initialization, four uncertain parameters are declared (nominal values and ranges presented in table 2).

Table 2. Uncertain parameters

Parameter	Value	Range
Tank mass multiplier	1	0-1
Panel rotation angle	0	0-2π rad
Panel damping ratio multiplier	1	0.85-1.15
Panel frequency multiplier	1	0.95-1.05

Regarding the summation of the spacecraft body's moments of inertia, the inertia matrix is calculated after taking the value of uncertain parameters into account, which results in an approximation of the real value for Sentinel-2B. In the nominal case, the inertia matrix J for the entire spacecraft has a value as follows:

$$\mathbf{J} = \begin{bmatrix} 998.50 & 15.044 & 0 \\ 15.044 & 1628.9 & 0 \\ 0 & 0 & 1689.6 \end{bmatrix}$$

2.1 Reference Frames

We will be using four reference frames throughout this paper, which are sufficient to describe the dynamics of the system. The first one is the Earth Centered Inertial (ECI, or "I") frame, whose origin is defined in the Earth's center of mass, with the z axis aligned with the mean North pole, the x axis with the mean vernal equinox at some epoch (here: J2000.0), and the y axis completing the right-handed orthogonal system. This is the only inertial frame, with the three other frames being defined to it.

The second one is Earth Centered Earth Fixed (ECEF, or "F"), which (disregarding precession and nutation) shares an origin and z axis with ECI, but the x-y axes are rotating with Earth. The rotation matrix $\mathbf{R}_{FI}$ can be formulated as a simple rotation around the z axis, with the angle as the product of Earth's rotation rate and the time passed since the ECI epoch. For modeling the planet and converting between ECEF and LLA (geodetic latitude, longitude, altitude), the paper uses the WGS84 reference ellipsoid.

The third frame is Local Vertical Local Horizontal (LVLH, or "L"), which is a local frame with an origin that is fixed to the center of mass of the spacecraft. The z axis points in the direction of the nadir (towards the center of mass of the Earth), the y axis to the negated normal vector of the orbital plane, and the x axis completing the right-handed orthogonal system. This is convenient for declaring the rotation matrix $\mathbf{R}_{LI}$ in simulations, as the nadir vector is the same as the negated unit ECI position vector, while the normal vector of the orbital place is the same as the unit cross product of the ECI position ($\mathbf{r}^I_{BI}$) and velocity ($\mathbf{v}^I_{BI}$) vectors. The transformed rotation matrix $\mathbf{R}_{LF}$ can also be defined with ECEF vectors and the WGS84 Earth rotation rate $\boldsymbol{\omega}_\oplus$, using the orthogonal basis vectors $\hat{\mathbf{o}}_i$:

$$\begin{aligned} \mathbf{o}_1 &= \mathbf{o}_2 \times \mathbf{o}_3 \\ \mathbf{o}_2 &= -\mathbf{r}^F_{BF} \times \left(\mathbf{v}^F_{BF} - \mathbf{r}^F_{BF} \times \boldsymbol{\omega}_\oplus\right) \\ \mathbf{o}_3 &= -\mathbf{r}^F_{BF} \\ \mathbf{R}_{LF} &= [\hat{\mathbf{o}}_1 \quad \hat{\mathbf{o}}_2 \quad \hat{\mathbf{o}}_3] \end{aligned} \tag{1}$$

Finally, the Body frame ("B") is defined with its origin fixed to the center of mass of the orbiting body, and its orientation fixed to the principal axes of the spacecraft.

2.2 Equations of Motion

Sentinel-2B occupies a highly inclined, circular orbit at 790 km altitude. The orbital dynamics of the satellite are described with two sets of differential equations, one for the ECEF position vector, and another for the body-frame velocity vector. Due to the rotation of the ECEF frame, there are also centrifugal and Coriolis components in the dynamics (Markley and Crassidis (2014)).

$$\begin{aligned} \ddot{\mathbf{r}}^F_{BF} &= \dot{\mathbf{v}}^F_{BF} = \\ &= \mathbf{R}_{FB}\frac{\mathbf{f}^B}{m} - 2\boldsymbol{\omega}_\oplus \times \mathbf{v}^F_{BF} - \boldsymbol{\omega}_\oplus \times \left(\boldsymbol{\omega}_\oplus \times \mathbf{r}^F_{BF}\right) \end{aligned} \tag{2}$$

Initial conditions for all the states have been calculated by extracting position and velocity data from the reference spacecraft's two-line orbital elements, after solving Kepler's equation and converting from the perifocal frame.

Regarding the gravity field, we used a zonal harmonic expansion to the fourth degree to account for the non-spherical gravity field. This is due to Earth having a geoid shape with a non-uniform mass distribution, which has a significant effect over the timescale of the simulations.

Then, we derived the differential equations from the relative dynamics of rotating reference frames and the kinematics of quaternions. Including the body-frame torques $\boldsymbol{\tau}^B$ and reaction wheel angular momentum $\mathbf{H}_{rw}$ in the equation, the angular velocity of the body frame with respect to the inertial frame can be expressed as:

$$\dot{\boldsymbol{\omega}}^B_{BI} = \mathbf{J}^{-1}\left[\boldsymbol{\tau}^B - \boldsymbol{\omega}^B_{BI} \times \left(\mathbf{H}^B_{rw} + \mathbf{J}\boldsymbol{\omega}^B_{BI}\right)\right] \tag{3}$$

Using a scalar-first convention and defining $\mathring{\boldsymbol{\omega}}^B_F$ as a quaternion with a zero scalar element, the kinematics of the quaternion between the fixed and body frames can be expressed as a single quaternion product. Notice how the quaternion is defined as a rotation between the ECEF and Body frames, in order to reduce model complexity.

$$\dot{\mathbf{q}}_{BF} = \frac{1}{2}\mathbf{q}_{BF} \circ \mathring{\boldsymbol{\omega}}^B_{BF} \tag{4}$$

Initial conditions for all rotation states are defined for a nadir-pointing case and zero angular velocity with respect to the local frame.

2.3 Disturbing Forces and Torques

There are numerous external and internal factors disturbing the motion of bodies in space through small forces and torques, whose magnitude and dynamics are dependent on both position and time. In Low Earth Orbit, the sources of main disturbing torques are aerodynamics, magnetism, and gravity. Solar radiation pressure is excluded from modeling to increase simulation speed, as it is a relatively minor effect in the selected altitude range. Torque models are further detailed in Markley and Crassidis (2014).

Gravity Gradient Torque Any non-symmetrical rigid body in a gravity field is subject to gravity-gradient torque, which is an effect that tries to align the principal axis of minimum inertia of the spacecraft with the nadir vector ($\mathbf{n}^B$). Assuming the gravity field to be spherically symmetric (standard parameter μ), it can be approximated as:

$$\boldsymbol{\tau}_{gg}^B = \frac{3\mu}{|r_{BF}^F|^3}\mathbf{n}^B \times \mathbf{J}\mathbf{n}^B \tag{5}$$

Magnetic Torque It is often the case for spacecraft that they have some magnetic dipole moment m_M, roughly estimated as a multiple (here: 1e-3 Am^2kg^{-1}) of the spacecraft mass in a random direction. This could be a result of residual magnetism from the on-board equipment, or electric current passing through a loop. In the magnetic field ($\mathbf{B}^F$) of Earth, which can be approximated to a desired degree using WMM2020, this generates a torque:

$$\boldsymbol{\tau}_m^B = \mathbf{m}_M \times \mathbf{R}_{BF}\mathbf{B}^F \tag{6}$$

Aerodynamic Torque One way to approximate drag is to consider the spacecraft to be a collection of flat plates, each with surface area s_i and surface normal vector $\mathbf{n}_i$. Since the atmosphere is rotating with the Earth, an "air speed" $\mathbf{v}_{rel}$ is also defined. Then, incident angles can be calculated for each of the plates, which allows for cancelling out the non-contributing ones. The total aerodynamic torque can then be calculated as the sum of individual forces and moment arms ($\mathbf{r}_{CP}$) on each of the plates making up the spacecraft:

$$\boldsymbol{\tau}_{ae,i} = \mathbf{r}_{CP} \times \left(-\frac{1}{2}\rho c_D s_i v_{rel}^2 \max\left\{\cos\theta_i, 0\right\} \cdot \hat{\mathbf{v}}_{rel}\right) \tag{7}$$
$$\mathbf{v}_{rel} = \mathbf{v}_{BF}^B \qquad \cos\theta_i = \mathbf{n}_i \cdot \hat{\mathbf{v}}_{rel}$$

In the equation, there are two variables: the drag coefficient of a flat plate ($c_D = 1.28$) and the atmospheric density (ρ). We used NRLMSISE-00 for the latter, which also takes into account the ionization of the upper atmosphere to give valid densities and temperatures up to 1000 km in altitude. We managed to significantly speed up calculation speed by using averaged values for parameters such as year, day, magnetic flux data, which are relatively constant over the simulation timescale (minutes).

2.4 Flexible Appendage

The spacecraft has a solar panel attached to one side of the body, which acts as a flexible appendage, disturbing its attitude. We modeled the panel as a flexible beam element constrained in the connection point with the spacecraft, based on the work of Alazard and Cumer (2018) and Alazard and Sanfedino (2020). Its properties are illustrated on figure 1, where the dynamics involve motion in just one rotation and one translation axis. Considering a Young modulus of E = 150 GPa (an approximation for single-crystal silicon in the panel), a state-space model of the appendage can be built with linear and angular acceleration in the connection point P as inputs, and reaction forces and torques in the same point as outputs.

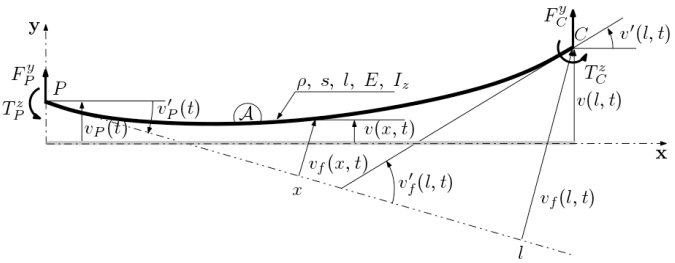

Fig. 1. Pure flexion (Alazard and Cumer (2018))

Since the full nonlinear model already incorporates the rigid dynamics of the panel, we separated those components from the resulting state-space model, so we can include the purely flexible appendage model without touching other parts of the spacecraft dynamics. This had the added benefit of respecting the modularity of the Simulink model. The flexible characteristics of the appendage for the nominal case are presented in table 3.

Table 3. Flexible characteristics

Frequency (rad/s)	Damping coeff.
17.2702	0.1
108.836	0.1
311.149	0.1
1383.16	0.1

2.5 Reaction Wheels

On most modern spacecraft, the primary instruments for attitude control actuation are reaction wheels. They are essentially torque motors with a high inertia rotor which can spin in either direction and can provide one axis of control. In the model, we are using one reaction wheel for each of the spacecraft's principal axes. For redundancy, an additional fourth wheel is added diagonally, at 45 degrees rotation to the three orthogonal ones (NASA Standard configuration). We applied the pseudoinverse distribution law to determine how much torque each wheel should contribute for control in 3 axes.

The driving motor of a single wheel is modeled as a low-pass filter with a cutoff frequency of 100 rad/s. Wheel friction is modeled as a sum of viscous ($k_v = 10^{-6}Nms$) and Coulomb ($k_c = 10^{-3}Nm$) components, and is dependent on the rotation rate of the wheel, ω^w. This rotation rate is directly related to the nominal torque, which can be expressed as the difference between drag torques and the motor torque. The axial moment of inertia of the wheel $J_w = 0.2kgm^2$ is taken from catalog data for a wheel with 0.3 Nm of maximum torque, 50 Nms capacity, and 3850 rpm maximum rotation speed.

$$\dot{\omega}^w = J_w^{-1}\tau_{nom}^w \qquad \tau_{nom}^w = \tau_{mot} - k_v\omega^w - k_c\text{sign}\left(\omega^w\right) \tag{8}$$

We modeled the microvibration environment of the wheel based on Kim (2014). In the wheel's rocking frame, N harmonic disturbances affect the wheel, which present as forces and torques in the x-y plane which are added to the nominal values. The parameters $a_i^{f,t}$ and h_i are the same as the ones used in the paper (which are estimated from experimental data), while $\phi_i^{f,t}$ are random phase angles.

$$\begin{bmatrix} F_i^x \\ F_i^y \\ \tau_i^x \\ \tau_i^y \end{bmatrix} = \begin{bmatrix} a_i^f(\omega^w)^2 \sin\left(h_i\omega^w t + \phi_i^f\right) \\ a_i^f(\omega^w)^2 \cos\left(h_i\omega^w t + \phi_i^f\right) \\ -a_i^t(\omega^w)^2 \cos\left(h_i\omega^w t + \phi_i^t\right) \\ a_i^t(\omega^w)^2 \sin\left(h_i\omega^w t + \phi_i^t\right) \end{bmatrix} \tag{9}$$

3. CONTROL DESIGN

Using this model, we built a control loop that consists of a state estimator with sensor models, a trajectory generator using sensor measurements, and a controller that calculates desired torques to be delivered by the reaction wheels. The linearized equations of rotational motion serve as the basis of control design, defined as follows:

$$\ddot{\boldsymbol{\theta}} = \dot{\boldsymbol{\omega}} = \mathbf{J}^{-1}\left(\boldsymbol{\tau}_{rw}^* + \boldsymbol{\tau}_{flex}^*\right) \tag{10}$$

In which the linearized reaction wheel torques ($\boldsymbol{\tau}_{rw}^*$) are free of vibrations and friction (but still have transient behaviour), while the linearized flexible dynamics ($\boldsymbol{\tau}_{flex}^*$) only respond to external torques (but not forces).

3.1 State Estimation

To estimate the states, four states are measured and then mixed with normally distributed random noise (characteristics presented in table 4). ECEF position is measured with GPS, Body-frame velocity with integrated accelerometer, body-frame angular velocity with a drifting gyro, and Euler angles with a star tracker.

Table 4. Noise Characteristics or Sensors

Sensor	Mean	Variance	Sample Time (s)
Gyro	0 rad/s	1e-13	0.01
Gyro Drift	0 rad/s^2	1e-18	0.01
Star Tracker	0 rad	1e-11	0.1
Accelerometer	0 m/s^2	1e-7	0.01
GPS	0 m	1e-2	1

With these sensor measurements, we estimate all other states of the system by plugging them into the equations of motion. To handle sensor drift, the integrators driven by the gyro and the accelerometer are periodically reset with lower frequency measurements from the GPS and star tracker. The state estimator also has some time delay (0.01 s), which is modeled with a 5th order Padé approximant in the linear model. Outputs are smoothed with a first-older holder (to be replaced with a Kalman filter in the future).

The outputs of state estimation to be used the trajectory generation and the controller are ECEF position $\mathbf{r}_B^F$, ECEF velocity $\mathbf{v}_B^F$, body-frame angular velocity $\boldsymbol{\omega}_{BI}^B$, and the Euler angles $\boldsymbol{\theta}$. The angles are calculated from the rotation quaternion from the LVLH frame to the Body frame ($\mathbf{q}_{BL}$) and follow an XYZ rotation order, which makes the line-of-sight vector (body-frame "Z") independent of the yaw angle. This is beneficial for both trajectory generation (as pointing precision only requires two Euler angles) and operations (as the yaw angle becomes a free parameter).

3.2 Trajectory Generation

We implemented a quaternion-based algorithm for trajectory generation, which solves the following question: what is the quaternion $\mathbf{q}_{BL}$ that rotates the nadir vector $\mathbf{i}_3$ ("Z" base of LVLH) into the vector $\mathbf{r}_{target}$ that connects the position of the spacecraft $\mathbf{r}_B^F$ with the ground target r_T^F? The first vector corresponds to the line-of-sight vector where all Euler angles are zero, while the second vector defines the desired case. Using the previously defined sensor measurements to first determine the ECEF-to-LVLH rotation matrix, the desired quaternion can be calculated as follows.

$$\begin{aligned} \mathbf{r}_{target}^L = \mathbf{R}_{LF}\left(\mathbf{r}_{TF}^F - \mathbf{r}_{BF}^F\right) \qquad \mathbf{i}_3 = \begin{bmatrix} 0 & 0 & 1 \end{bmatrix}^T \\ \mathbf{q}_{BL} = \begin{bmatrix} 1 + \mathbf{i}_3 \cdot \mathbf{r}_{target}^L & \mathbf{i}_3 \times \mathbf{r}_{target}^L \end{bmatrix} \end{aligned} \tag{11}$$

After normalizing the quaternion, it is converted to Euler angle representation using an XYZ convention with the yaw angle set to zero, then multiplied with a polynomial smoothing factor. The derivatives of this polynomial at T=0 and T=150s are all zeroes up to the third order, which ensures continuity in the trajectory and significantly decreases the required control effort (Chen et al. (2000)).

In order to calculate the trajectory for the angular velocities, the measured position and velocity of the spacecraft are used to propagate its orbit 0.01 s ahead in time using the Bogacki–Shampine method on the orbital equations of motion. Then, the desired rotation quaternion is also calculated, normalized, and smoothed for the propagated states. Finally, both are rotated to represent ECEF-to-Body quaternions ($\mathbf{q}_{BF}$). We then applied first-order numerical differentiation to get $\dot{\mathbf{q}}_{BF}$, which was plugged into the inverted rotation kinematics to define the desired $\boldsymbol{\omega}_{BF}^B$.

3.3 PID Control

As a test case, we implemented a PID control loop with controller coefficients as shown in table 5. The control torque is calculated by substracting measured Euler angles ($\boldsymbol{\theta}_m$) and angular velocities ($\boldsymbol{\omega}_m$) from the desired trajectories ($\boldsymbol{\theta}_d$ and $\boldsymbol{\omega}_d$) to get error signals $\boldsymbol{\theta}_e(t)$ and $\boldsymbol{\omega}_e(t)$:

$$\boldsymbol{\tau}_c(t) = \mathbf{k}_P \cdot \boldsymbol{\theta}_e(t) + \mathbf{k}_I \int \boldsymbol{\theta}_e(t)dt + \mathbf{k}_D \cdot \boldsymbol{\omega}_e(t) \tag{12}$$

Table 5. PID Controller Coefficients

Controller	k_P	k_I	k_D
Roll	500	400	2000
Pitch	500	400	2000
Yaw	1e-1	1e-4	100

The coefficients were calculated by using the proprietary PID Tuner tool of Simulink on the time-delayed linearized equations of rotational dynamics to get a stable system response, then further tuning the resulting controllers to improve stability characteristics on the linearized system and pointing performance on the nonlinear system. Roll and pitch are more strictly controlled as they have the largest impact on pointing precision.

3.4 Nominal Control Performance

All simulations in this paper are carried out using an ode3 (Bogacki-Shampine) solver at a fixed step time of 1 ms, with a simulation length of 800 s. For testing the control loop, the satellite was initialized with two-line orbital elements measured during the morning pass, and then pointed at an off-track city nearby. This ensured a realistic test scenario with a large roll angle. After closely following the smooth portion of the trajectory, the designed controller produced an absolute performance error within the ±2 arcsec range for roll and pitch, and ±3 degree range for yaw (figure 2). This was achieved by also staying within the maximum torque range of the reaction wheels. In case of wheel failure, the smooth portion of the trajectory can be extended to further reduce the required torque. After intersecting the line-of-sight vector with the WGS84 reference ellipsoid, we determined the results to correspond to a ground error of less than 10 meters for the entire pass, which lasted several minutes and can be extended even further by proper timing of the maneuver.

4. PARAMETER UNCERTAINTY ANALYSIS

To verify the designed controller, it has to be robust with regards to parameter uncertainty. The targets of this analysis are the four variables that we have defined at the start of the paper (table 2). First, their effect is individually assessed on system stability, using Bode diagrams and pole-zero plots. We have found that the panel rotation angle is markedly different from the other three parameters, since it provides a way for flexible behaviour to be transferred from purely yaw dynamics to purely roll dynamics (and anything inbetween). This shows up as large dips on both Bode curves at the vibration frequencies. As such, this allows for defining two parameter sets for worst-case scenarios: one for purely yaw disturbances (0 rotation, Param 1), and another for purely roll disturbances (90 deg rotation, Param 2).

The remaining three parameter ranges are then sliced up with 10% intervals to form two cubes of potential parameter sets, one for each rotation angle. Then, all of the cases are analyzed in an exhaustive search to identify the case with the worst phase margin characteristics. These were found to be at the edges, as presented in table 6.

Table 6. Worst-case Parameter Sets

Parameter	Param 1	Param 2
Tank mass multiplier	0	0
Panel rotation angle (deg)	0	90
Panel damping ratio multiplier	0.85	0.85
Panel frequency multiplier	1.05	1.05

Two figures showcase the effect of uncertainty on the control loop's performance. Figure 4 presents Bode diagrams and pole-zero maps for both the yaw and the roll responses. Several systems are shown on the graphs at the same time, transforming the nominal case parameter set (blue) into the worst-case parameter set (red) in a linear manner. The main feature is the gradual loss of phase margin at the vibration frequencies as we move away from the nominal case, visible as a deepening dip on the phase diagrams. The poles migrating closer to the Re=0 axis is also noticeable.

Regarding performance in the nonlinear simulation (figure 3), little difference was found between the three cases, despite the controller retaining its tuning. This indicates that the control loop is sufficiently resilient to parameter uncertainty.

5. CONCLUSION

Overall, the classical PID has been proven sufficiently robust to uncertainty in the four selected parameters, with satisfactory results (±2 arcsec) in precise pointing using the high-fidelity simulation. Matching expectations, stability characteristics such as phase margin got worse, especially for roll response, but didn't affect system behaviour. Our next goal is to design an advanced control loop to further improve performance, by replacing the PID with an H_∞ or MPC-based controller, and designing a vibration-isolated camera platform with an additional inner control loop. This will then be followed by expanding the presented uncertainty analysis to more parameters in order to determine the most significant contributors to performance degradation, and carrying out a Monte Carlo campaign to further validate the designed control loop.

REFERENCES

Alazard, D. and Cumer, C. (2018). Satellite Dynamics Toolbox - Principle, User Guide and tutorials. Technical report, ISAE/DMIA/ADIS.

Alazard, D. and Sanfedino, F. (2020). Satellite dynamics toolbox for preliminary design phase. In *43rd Annual AAS Guidance and Control Conference*, volume 30, 1461–1472.

Chen, X., Steyn, W., and Hashida, Y. (2000). Ground-target tracking control of earth-pointing satellites. In *AIAA Guidance, Navigation, and Control Conference and Exhibit*, 4547.

Gasbarri, P., Monti, R., Campolo, G., and Toglia, C. (2012). Control-oriented modelization of a satellite with large flexible appendages and use of worst-case analysis to verify robustness to model uncertainties of attitude control. *Acta Astronautica*, 81(1), 214–226.

Kim, D.K. (2014). Micro-vibration model and parameter estimation method of a reaction wheel assembly. *Journal of Sound and Vibration*, 333(18), 4214–4231.

Markley, F.L. and Crassidis, J.L. (2014). *Fundamentals of spacecraft attitude determination and control*. Springer.

Preda, V., Cieslak, J., Henry, D., Bennani, S., and Falcoz, A. (2018). Robust microvibration mitigation and pointing performance analysis for high stability spacecraft. *International Journal of Robust and Nonlinear Control*, 28(18), 5688–5716.

Wang, W., Menon, P., Bates, D., and Bennani, S. (2010). Robustness analysis of attitude and orbit control systems for flexible satellites. *IET control theory & applications*, 4(12), 2958–2970.

Xiao, B., Hu, Q., and Zhang, Y. (2011). Adaptive sliding mode fault tolerant attitude tracking control for flexible spacecraft under actuator saturation. *IEEE Transactions on Control Systems Technology*, 20(6), 1605–1612.

Xiao, B., Yin, S., and Kaynak, O. (2016). Attitude stabilization control of flexible satellites with high accuracy: An estimator-based approach. *IEEE/ASME Transactions on Mechatronics*, 22(1), 349–358.

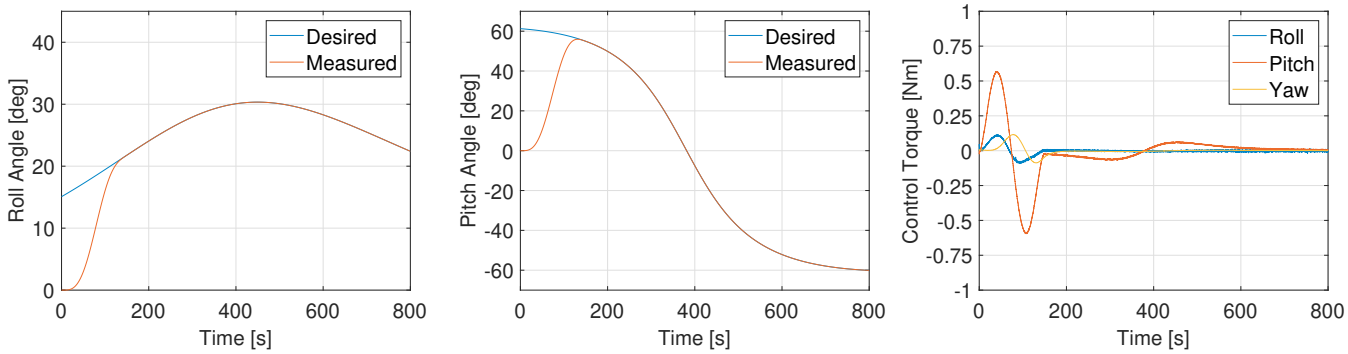

Fig. 2. Control performance of the PID in the nonlinear simulation (nominal case)

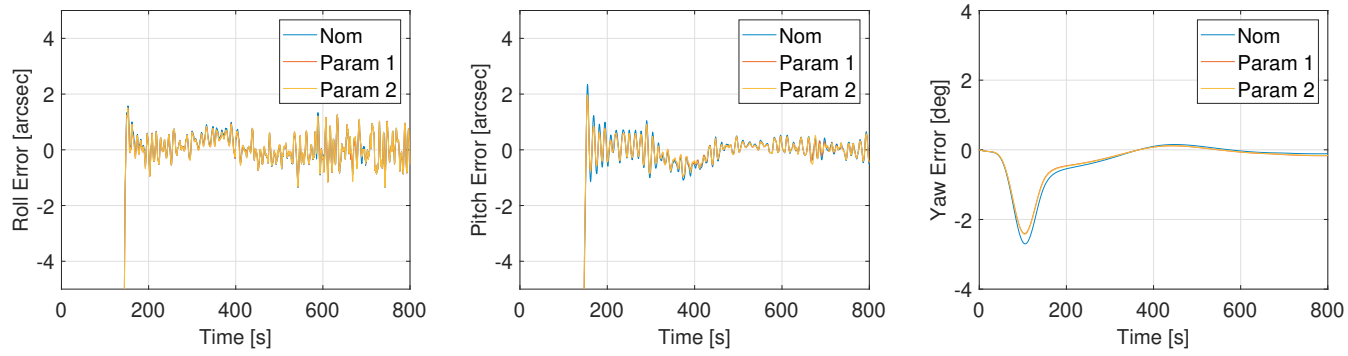

Fig. 3. Control performance of worst-case models in the nonlinear simulation compared to nominal case

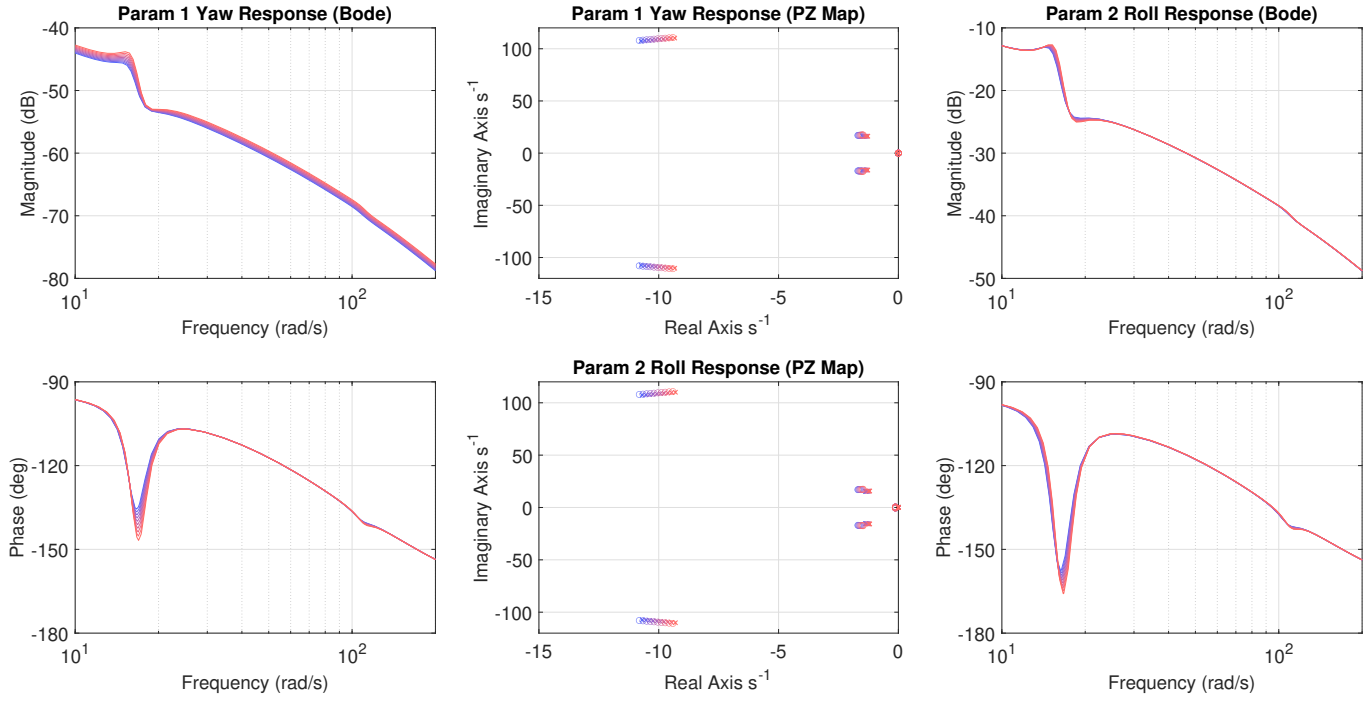

Fig. 4. The effect of uncertainty on linearized yaw and roll dynamics for parameter sets between nominal (blue) and worst-case (red)